Taylor & Francis
Taylor & Francis Group

Prediction of distortions and pattern allowances during sand casting of a steel bracket

D. Galles & C. Beckermann

Taylor & Francis
Taylor & Francis Group

Prediction of distortions and pattern allowances during sand casting of a steel bracket

D. Galles and C. Beckermann

Department of Mechanical and Industrial Engineering, University of Iowa, Iowa City, IA, USA

ABSTRACT

Mechanical interactions between the casting and mould generate unwanted distortions and lead to dimensional inaccuracies. In this study, the effects of mould expansion and mould restraint are investigated through sand casting experiments involving a U-shaped steel bracket. Distortions are quantified by *in situ* measurements of the evolution of the gap opening between the bracket legs. Mould expansion is observed immediately after filling. Outer mould restraint prevents distortions in the bracket legs until the time of mould fracture, after which the legs are pushed outward. The experiments are simulated using a sequential thermo-mechanical coupling. The steel and bonded sand are modelled using previously calibrated elasto-visco-plastic and Drucker–Prager Cap constitutive laws, respectively. Excellent agreement between measured and predicted pattern allowances (PA) is obtained. Distortions are greatly under-predicted unless mould fracture is considered. Variations in the packing density of the moulds are also shown to have an impact on PA.

1. Introduction

During sand casting, mechanically induced stresses are created when some part of the mould contacts the casting. These contact interactions may generate distortions, which in turn influence pattern allowances (PA):

$$PA\,[\%] = \frac{feature\ length_{initial} -\ feature\ length_{final}}{feature\ length_{initial}} \times 100$$

(1)

Equation (1) defines the per cent change for a particular casting dimension (i.e. feature length) that occurs from the onset of filling (initial subscript) until the casting cools to room temperature (final subscript). Positive PA represent a reduction in the feature length. The pattern-maker's shrink is a special, well-defined pattern allowance that defines dimensional changes that are due to thermal strains only (e.g. the pattern allowance for a low alloy steel is approximately 2.1%) and can be viewed as a point of reference; any deviation from the patternmaker's shrink represents a distortion.

Distortions create inefficiencies throughout the casting process that can adversely impact lead times and generate considerable waste. For example, pattern design is often characterised by a time-consuming tri-al-and-error process in which several design iterations are required. In addition, PA are sensitive to process conditions (e.g. mould packing density) that must be

carefully controlled. Otherwise, post-casting operations such as straightening, machining, or welding may be needed to meet dimensional requirements. Finally, distortions generated near the end of solidification may cause hot tears, requiring the casting to be scrapped. Mitigation of these problems will lead to efficiently produced, high quality as-cast parts.

Mechanically induced distortions are created by either mould expansion or mould restraint. Mould expansion occurs during filling and throughout solidification when the sand mould rapidly heats and expands into the mould cavity, reducing the casting volume. Galles and Beckermann [1] found that this expansion is not only due to thermal expansion of the bonded sand, but also sand dilation (i.e. the volumetric expansion of granular media due to a shear force). Mould restraint generally occurs at later times, after the casting has solidified, during which the mould impedes thermal contractions in the casting and generates distortions.

In order to predict casting distortions and PA, the combined effect of mould expansion and mould restraint must be considered. Mould restraint has been the focus of several experimental studies [2–6] that involved casting slender bars in sand moulds. Thermal contractions in the bars were constrained (usually with the aid of flanges) to generate distortions during cooling. Most of these studies were experimental, as only Motoyama et al. [6] attempted to predict the observed distortions

CONTACT C. Beckermann ✉ becker@engineering.uiowa.edu

in an aluminium bar through a finite-element stress analysis. Mould expansion has received less attention, as the only comprehensive study was performed by Galles and Beckermann [1], who calibrated Drucker–Prager Cap constitutive model parameters from *in situ* casting experiments. The only study to consider both mould expansion and mould restraint was performed by Peters et al. [7], who cast hollow cylinders with varying wall thicknesses in a sand mould. Inner diameter PA were measured and then predicted by a finite-element stress analysis. Distortions were attributed to both mould expansion and mould restraint. However, because dilation was not considered, distortions created by mould restraint may have been over-predicted.

The increase in computational speeds over the past 20 years has enabled the prediction of distortions for production steel castings in a practical manner. Large castings with complex geometries can now be simulated in less than a day. Unfortunately, the accuracy of the predictions remains questionable. This is largely due to the uncertainty of the high temperature bonded sand properties. Several researchers have contributed in this area, using mechanical testing to determine high temperature properties, including compressive strength,[8, 9] tensile strength[9] and elastic modulus.[10] Unfortunately, these measurements alone are not sufficient to completely characterise the high temperature behaviour of bonded sand, which exhibits pressure-dependent yielding. Such materials require testing methods typically reserved for geological materials. In that respect, Saada et al. [11] performed the most comprehensive study on bonded sand by conducting triaxial, uniaxial compression, isotropic compression, and die pressing tests on green sand at elevated temperatures. These data were then used to calibrate Cam Clay and Hujex constitutive models for use in finite-element stress analyses.

The aforementioned studies contributed invaluable data needed to predict casting distortions. Unfortunately, the harsh conditions encountered during casting may have a strong influence on the mechanical properties. In particular, the high heating/cooling rates seen during casting cannot be recreated by mechanical testing. For this reason, mechanical testing data may not be suitable to calibrate model parameters used for the prediction of casting distortions. Rather, representative data should be acquired from *in situ* testing. For example, the mechanical steel properties developed through the *in situ* measurements of Galles and Beckermann [1] were found to be considerably different from those determined from previous mechanical testing.

In the present work, distortions are measured *in situ* during casting experiments, which are then simulated in order to predict PA for steel sand castings. For the experiments, a U-shaped steel bracket is produced in a no-bake bonded sand mould. By utilising LVDTs (Linear Variable Differential Transformers) connected to quartz rods, distortions created by both mould expansion and mould restraint are quantified. PA are measured at several feature locations. For the simulations, a sequential temperature-displacement coupling is adopted. Using commercial casting simulation software, temperatures are calculated in the casting and mould and subsequently inputted into a finite-element stress analysis. The steel is modelled using an elasto-visco-plastic constitutive law, whereas the bonded sand employs the Drucker–Prager Cap model. Constitutive data-sets for the steel [12] and bonded sand [1] were previously calibrated with *in situ* measurements. The quasi-brittle behaviour of the mould and the packing density of the mould are shown to have a strong impact on the predicted PA.

2. Description of experiments

2.1. Experimental set-up

The geometry and experimental set-up for the U-shaped bracket are depicted in Figure 1(a) and (b), respectively. The bracket is comprised of two legs and a top section. Dimensions are shown in mm. The outer mould dimensions are 254 mm (length) × 254 mm (width) × 75 mm (height) for the cope and 254 × 254 × 230 for the drag. Rather than using a core, the drag was built as a single piece. The region of bonded sand located between the bracket legs is henceforth referred to as the 'inner mold' (see the light-red shaded section in Figure 1(b)). A horizontal parting line was utilised and is located at the top surface of the bracket. A simple gating system consisting of a sprue (25 mm radius × 50 mm height) and pouring cup (which also served as a feeder) was used. Refractory bricks were utilised to provide a heat transfer barrier between the drag and foundry floor. All measurements described below (i.e. displacement, temperature) were taken on the vertical casting mid-plane as shown in Figure 1(b) at a sampling rate of 1 Hz.

As the casting cools, the inner mould will constrain thermal contractions in the bracket and likely generate distortions. In order to quantify distortions due to this effect, the temporal evolution of the outer length (see Figure 1(b)) was measured using two identical assemblies consisting of a quartz rod and LVDT. For each assembly, one end of the rod was bulged into a spherical shape (to firmly anchor the rods into the steel and minimise slippage [1]) using an oxy-acetylene torch and inserted through a pre-drilled hole in the drag. The bulged end extended approximately 3 mm into and 5 mm above the bottom of the mould cavity. The other end of the rod was connected to an Omega® LD620–5 LVDT. The other assembly was inserted through a pre-drilled hole on the other side of the drag. The temporal evolution of the outer length was determined by adding the LVDT measurements together.

Using Type K thermocouples, temperatures were measured in the inner mould midway between the

(a) Casting Geometry   (b) Schematic at vertical mid-plane
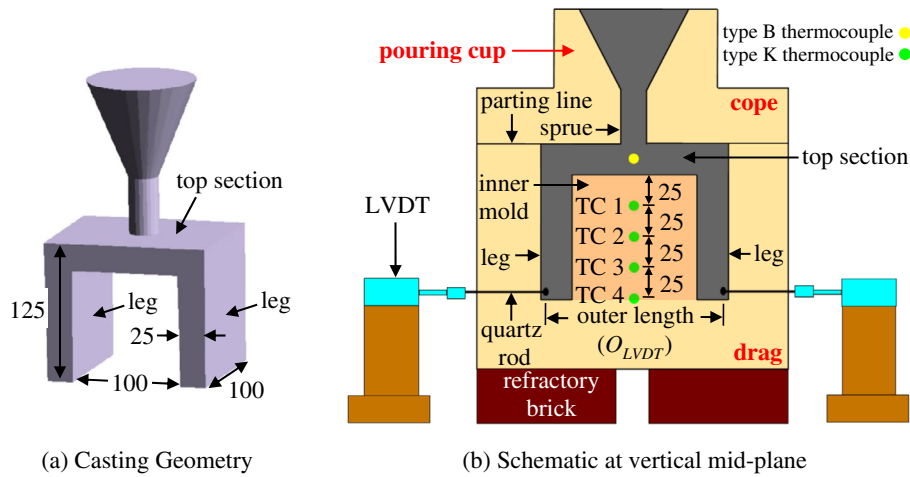
Figure 1. Casting geometry (a) and experimental schematic (b) for the bracket experiments. The bracket consisted of a top section and two legs. The region between the bracket legs (light red) is termed the 'inner mold'. The temporal evolution of the outer length was measured by LVDTs. All dimensions in mm.

Table 1. Experimental casting chemistries. The remaining balance is %Fe.

Experiment	%C	%Si	%Mn	%P	%S	%Cr	%Mo	%Ni	%Al	%Cu
1	0.33	0.59	0.39	0.015	0.020	0.01	0.01	0.01	0.069	0.03
2	0.14	0.38	0.26	0.093	0.013	0.02	0.01	0.01	0.001	0.07
3	0.30	0.57	0.41	0.031	0.026	0.01	0.00	0.00	0.056	0.01
4	0.27	0.23	0.61	0.012	0.009	0.63	0.19	2.0	0.021	0.04

bracket legs at 25, 50, 75 and 100 mm (denoted TC1, TC2, TC3, and TC4, respectively) from the bottom surface of the top section, as shown in Figure 1(b). Additionally, temperature was measured in the steel using a type B thermocouple, which was encased in a quartz tube and inserted underneath the sprue (albeit slightly offset to prevent inertial forces from breaking the quartz tube during filling).

To build the mould components (i.e. cope, drag, and pouring cup), Unimin® IC55 silica lake sand was bonded with a phenolic urethane no-bake (PUNB) binder system. The binder comprised 1.25% of total mould weight and was mixed using a 55:45 ratio of part 1 (PEPSET® 1000) to part 2 (Techniset® 6435). All mould components were hand-packed.

2.2. Casting procedure

Experimental casting trials were performed at the University of Northern Iowa's Metal Casting Center. In total, four brackets were cast. The target chemistry was ASTM A216 grade WCB carbon steel. Experimental casting chemistries are shown in Table 1. The castings were poured from a 250 lb heat and prepared in an induction furnace. The molten steel was heated to approximately 1700 °C in the furnace. The castings were poured within four hours after building the moulds. Immediately before pouring, any slag was removed from the ladle. Weights were applied on the top of the cope to prevent it from shifting during and after filling.

2.3. Experimental results

The measured LVDT displacements are plotted in Figure 2 as the change in outer length (see Figure 1(b) for feature location) vs. time. Results are shown on complete (60,000 s), 5000 s, and 1000 s time scales in Figure 2(a), (b), and (c), respectively. The complete time scale represents the approximate time needed to cool the casting to room temperature. The reduced time scales (5000 and 1000 s) are needed to observe events that are difficult to see on the complete time scale. Each curve represents a separate experiment. Note that for experiment 3 (green curve), one of the quartz rods failed at approximately 1000 s. After this time, the curve was recreated using data from experiment 1 and is represented by a dashed line.

The curves in Figure 2 contain several characteristic features which give insight as to when casting distortions occurred and what caused them (i.e. mould expansion or mould constraint). During the initial 50 s, the outer lengths decreased some amount between 0.1 mm (Experiment 3) and 0.4 mm (Experiment 4). This reduction was caused by mould expansion, which was induced by rapid heating of the bonded sand near the mould–metal interface. At these early times, the steel had not yet reached coherency and could be easily displaced by the expanding mould. The consequence of mould expansion, which impacted the entire casting surface, was a volumetric reduction of the casting; the displaced molten steel was forced back into the pouring cup. At approximately 100 s, the outer length increases, as the bracket legs were pushed apart. Such an outward push
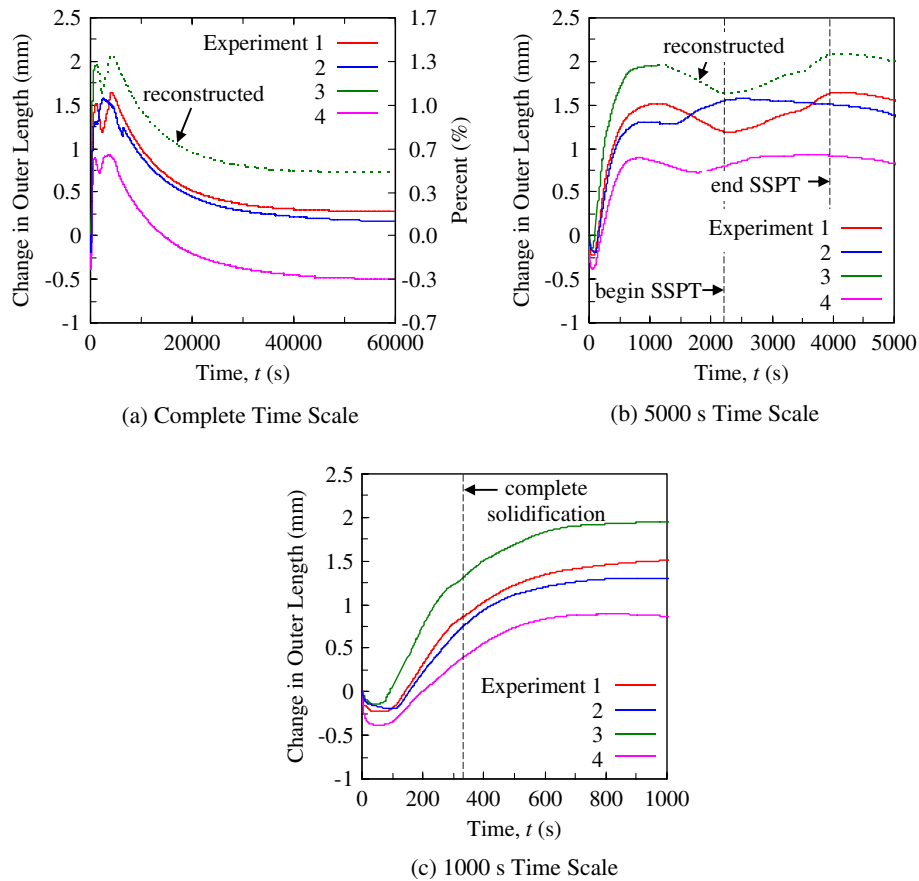
Figure 2. Measured change in outer length for the bracket experiments plotted on complete (a), 5000 s (b), and 1000 s (c) time scales. The vertical dashed lines in (b) denote the beginning and end of the SSPT from austenite to α-ferrite and pearlite for experiment 1.

was only possible if the inner mould acted as a fulcrum, about which each leg pivoted. Complete solidification of the bracket (approximated from the measured cooling rate in the steel) occurred around 325 s (denoted by the vertical dashed line in Figure 2(c)), after which the outer length increased by roughly 0.5 mm until reaching a local maximum at approximately 1000 s. During this period, the fully solid bracket was still very weak and could be easily distorted by inner mould restraint. The LVDT curves begin to decrease shortly after 1000 s, as the cooling steel had gained sufficient strength and could now overcome the core restraint, pulling the bracket legs inward. This decrease continued until a local minimum, which denotes the onset of the solid state phase transformation (SSPT) in the steel from austenite to pearlite and α-ferrite. The subsequent increase in outer length was the result of the volumetric expansion in the steel associated with the phase transformation. The end of the phase transformation is manifested as a local maximum in the curves, after which the outer lengths decreased monotonically until room temperature. The beginning and end of the phase transformation for experiment 1 are denoted as vertical dashed lines (labelled 'begin SSPT' and 'end SSPT'). Depending on the experiment, the beginning and end times of the transformation varied, which can be attributed to differences in casting chemistries. For example, the phase transformation for experiment 2 commenced

long before those in the other experiments. The carbon content (see Table 1) for experiment 2 (0.14%) was considerably lower than the other experiments (0.27–0.33%) and likely had an impact on the temperatures at which the phase transformation began and ended. Other differences can be seen in Table 1 (i.e. %P for Experiment 2, %Ni for Experiment 4) that may have also impacted the phase transformation temperatures. After the SSPT was complete, the outer lengths decreased at the same rate (i.e. all curves are parallel) until room temperature. This observation suggests that all changes in the outer length after the phase transformation were caused by thermal strains (the thermal strain simulations will validate this hypothesis).

Noticeable scatter in the curves can be seen between individual experiments, as the outer length increased to almost 2 mm for experiment 3 after 1000 s as opposed to only 0.9 mm for experiment 4. These differences can likely be attributed to the packing density (the effect of packing density on predicted distortions is demonstrated below), which signifies the importance of controlling process variables. Recall that the moulds were hand-packed, leading to considerable uncertainty in the bulk density of the moulds.

In addition to the LVDT measurements, PA were measured for the leg thickness (L), gap opening (G), and outer length (O) on two outer and one inner planes, as shown

(a) Bracket Feature Locations

(b) Measured Pattern Allowances
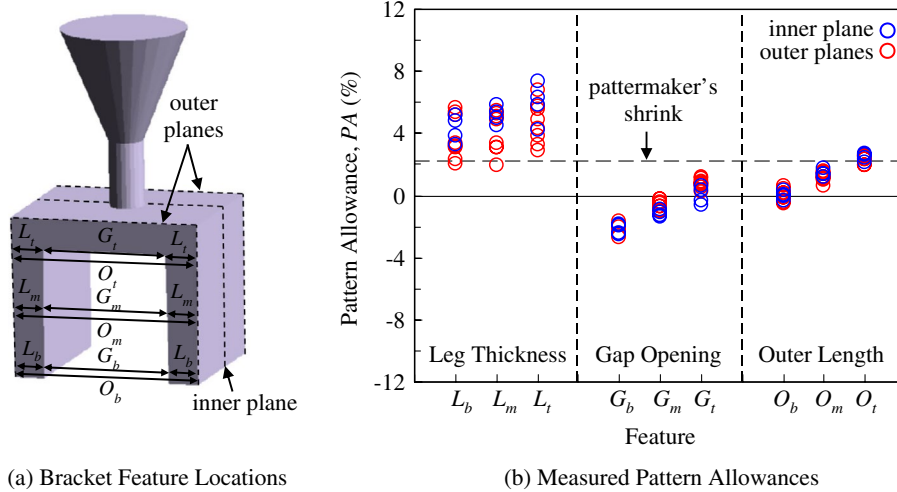
Figure 3. PA were measured on inner and outer planes for the features shown in (a). Standard deviations for the measurements in (b) ranged from 0.1–0.2 mm.

in Figure 3(a). The subscripts indicate that the measurements were taken at the bottom (b), mid-height (m), or top (t) of the bracket legs. The bottom and top measurements were taken 5 mm above the bottom of the bracket legs and 5 mm below the bottom surface of the top section, respectively. The measured PA are shown in Figure 3(b). The patternmaker's shrink (i.e. pattern allowance due to thermal strains) is indicated in Figure 3(b) by a vertical dashed line and serves as a reference. Any deviation from this line represents a distortion. Keep in mind that a larger pattern allowance signifies a greater reduction in the feature length during casting. In general, the leg thickness (L) PA exceeded the patternmaker's shrink. The additional reduction (over the patternmaker's shrink) in L was caused by mould expansion during solidification, which 'squeezed' the legs and reduced their thicknesses. Then, from the end of solidification until cooling to room temperature, L thermally contracted unconstrained and was reduced an additional amount equal to the patternmaker's shrink. On average, the inner plane PA (blue symbols) were slightly larger than the outer plane PA (red symbols) for L. This is because the outer planes solidified before the inner planes. Once the solidifying steel becomes coherent (i.e. can transmit stresses), any further reduction in L due to mould expansion is unlikely. Hence, shorter solidification times will lead to smaller PA for L, which also explains why the average pattern allowance for L_t is greater than those for L_b and L_m. The leg thickness pattern allowance measurements also contain more scatter than the gap opening or outer length measurements. The standard deviation for the measurements ranged from 0.1 to 0.2 mm, depending on surface roughness. This variation caused the most scatter in the PA for L, whose nominal dimension (25 mm) is much smaller than G (100 mm) and O (150 mm). For the gap opening (G), all measured PA were less than the patternmaker's shrink. In contrast to the PA for L, mould expansion caused G to increase

(this can be visualised from Figure 3(a)), reducing the pattern allowance. In addition, inner mould constraint pushed the legs outward and reduced the PA further. As a result, the combined effect of inner mould expansion and inner mould constraint led to negative PA for the majority of the gap opening features. In other words, the majority of these feature lengths increased during casting. In general, the PA for $G_b < G_m < G_t$, which should be expected as long as the bracket legs remain planar. The inner plane PA were somewhat smaller than the outer plane PA for G. This difference can again be attributed to local solidification times in the bracket. On average, the outer length (O) pattern allowance measurements are closer to the patternmaker's shrink than those for L or G. In particular, O_t appears to have experienced minimal distortions, as all the pattern allowance measurements are close to the patternmaker's shrink. However, it is clear from Figure 3(a) that $O = 2L + G$. Essentially, the addition of L and G 'cancelled out' distortions, resulting in pattern allowance measurements that were deceivingly close to the patternmaker's shrink.
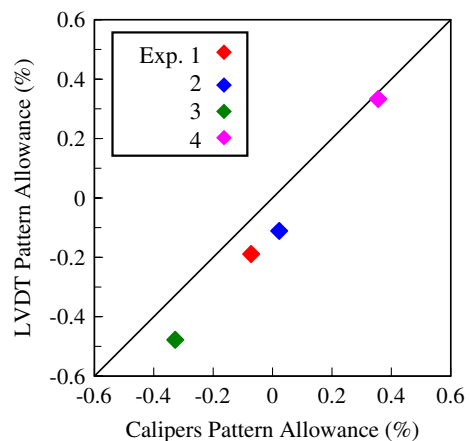
**Figure 4.** Comparison between the LVDT and calipers PA for feature O_b on the inner plane (see Figure 3).

From Figures 1(b) and 3(a), it can be seen that O_{LVDT} and O_b are the same feature. The negative change in inner diameter at 60,000 s (see Figure 2(a)) was used in the numerator of Equation (1) to determine the PA for O_{LVDT}. These values are compared to the PA for O_b in Figure 4. For $O_{LVDT} = O_b$, the symbol will fall on the 45° line in the figure. Experiment 4 (pink symbol) nearly falls on this line, whereas larger discrepancies between O_{LVDT} and O_b can be seen for the other brackets. These differences can be attributed to slippage between the quartz rods and casting during solidification, as explained by Galles and Beckermann [1]. To remedy this, the LVDT measurements will be adjusted slightly during the initial 50 s to match the callipers measurements. In general, these adjustments are minor and do not affect the overall shapes of the measurement curve. The main effect of the adjustments is that differences between the LVDT curves were minimised during the initial 50 s. All subsequent plots that show LVDT measurements will now use the adjusted curves (see Chapter 5), which are labelled appropriately.

3. Thermal simulations

Using the commercial casting software code MAGMASOFT®,[13] temperatures were calculated in the casting and mould from the time of filling until the casting cooled to room temperature. Virtual thermocouples were placed in the simulation model at the experimental locations. Predicted temperatures at these locations were later compared to the measured temperatures for validation. Simulation inputs included temperature-dependent thermophysical properties (i.e. density, specific heat, thermal conductivity) for the steel and bonded sand, as well as latent heat of solidification and the temperature-dependent solid volume fraction for the steel. The interfacial heat transfer coefficient (IHTC) governs the heat transfer across the mould–metal interface and accounts for the evolution of an air gap during cooling. Inclusion of the IHTC allows for a decoupling of the thermal-mechanical problem.

The input parameters were calibrated for PUNB bonded silica sand by Galles and Beckermann [1, 2] using a procedure described elsewhere.[14, 15] In general, the predicted and measured temperatures agreed reasonably well. The IHTC was then modified slightly, which resulted in excellent agreement between the measured and predicted temperatures, as shown in Figure 5(a) and (b) on complete and 2500 s time scales, respectively. Figure 5(c) illustrates the uneven solidification that is predicted in the bracket. It can be seen that the bottoms of the bracket legs are over 50% solidified at 25 s. Around

(a) Complete time scale

(b) 2500 s time scale
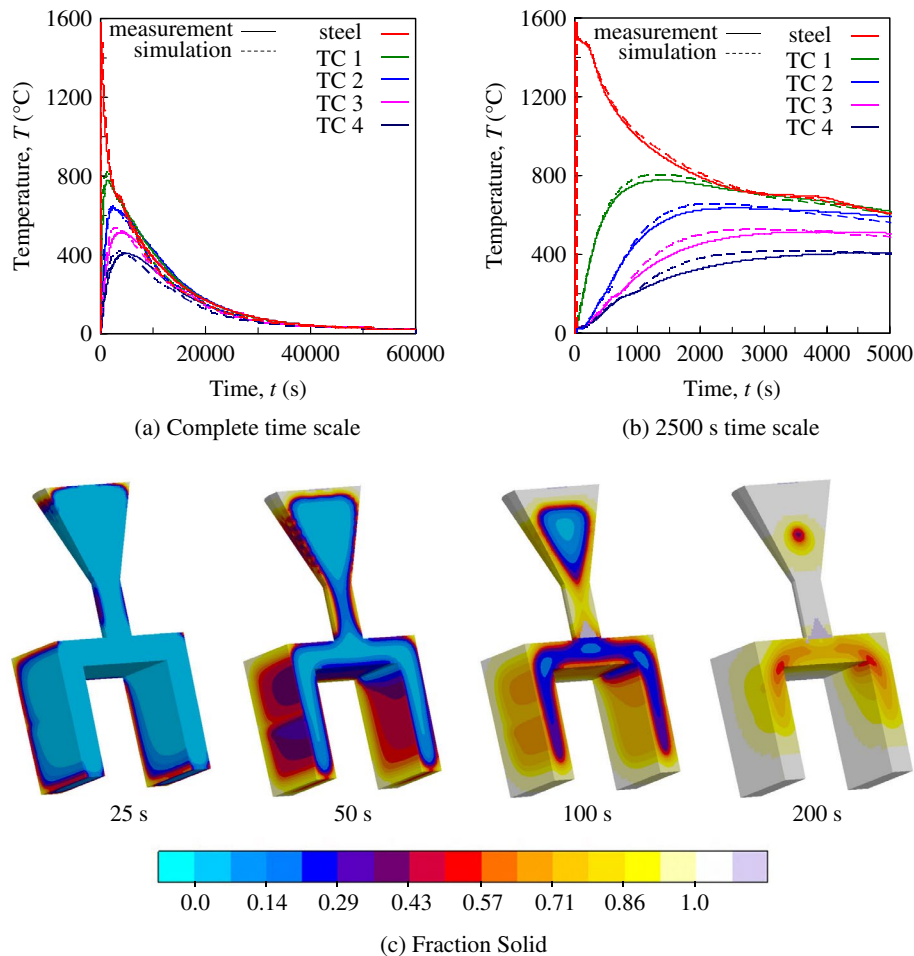
(c) Fraction Solid

Figure 5. Comparison between measured and predicted temperatures on complete (a) and 5000 s (b) time scales. The predicted fraction solid contours in (c) illustrate uneven solidification.
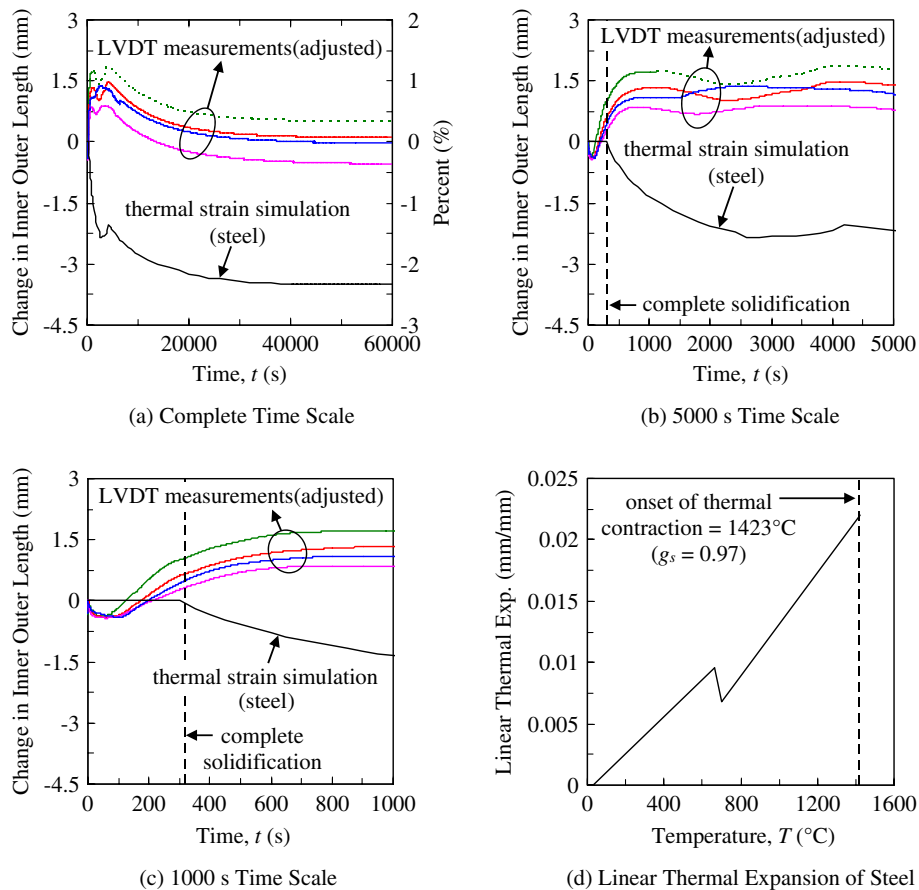
this time, the steel reaches coherency, after which minimal mould expansion can be expected. These predictions coincide with the LVDT measurements in Figure 2(c); the majority of the decrease in outer length occurs during the initial 25 s, after which minimal amounts are observed between 25 and 50 s. Temperature fields were written at a sufficient number of time steps (in order to ensure a smooth temperature profile at every node) and then copied onto the finite-element mesh.

4. Thermal strain predictions

Preliminary finite-element simulations calculated the thermal strains in the bracket. A comparison of these predictions with the LVDT measurements will reveal when distortions occurred and thus, provide invaluable insight to the mechanism that created them. The mould was excluded from the simulation in order to prevent any distortions due to mechanical interactions between the mould and bracket. Thus, only the bracket was simulated, for which minimal boundary conditions were specified to prevent rigid body translations or rotations. Young's modulus for the steel was set to a very low value (1×10^{-6} MPa), ensuring that negligible mechanical strains due to thermal stresses were predicted.

The predicted evolution of the outer length due to thermal strains is compared to the LVDT measurements on complete, 5000 and 1000 s time scales in Figures

6(a), (b) and (c), respectively. Thermal strains in the steel were calculated using the linear thermal expansion curve in Figure 6(d), which was calibrated by Galles and Beckermann.[12] The 'kink' in the linear thermal expansion curve at approximately 700 °C is included to predict dimensional increases associated with the SSPT. The onset of thermal contraction is based on the findings of Galles and Beckermann [12] and was set to $g_s = 0.97$. Hence, thermal strains will not be predicted until shortly before complete solidification. This can be seen in Figure 6(c), in which the thermal strain simulation curve begins to decrease at 300 s, about 25 s before complete solidification. Clearly, the measured outer length is distorted during this time frame (see Section 2 for a detailed explanation). From 100 to 300 s, the LVDT curves increased. Because the top section of the bracket had not yet started to thermally contract, the increase in outer length during this period can only be attributed to inner mould expansion (and not inner mould restraint). At 300 s, the onset of thermal contractions were predicted and pulled the legs inward. As a result, the thermal strain simulation curve decreases until a local minimum at approximately 2500 s, which represents the onset of SSPT. Prior to the thermal strain simulation, it was already obvious from the increasing LVDT curves that the outer length was distorted from 300 to 1000 s during the experiments. Now, by comparing the measured and simulated slopes of the curves after 1000 s, it is also evident that distortions were

(a) Complete Time Scale

(b) 5000 s Time Scale

(c) 1000 s Time Scale

(d) Linear Thermal Expansion of Steel

Figure 6. Comparison between the predicted change in outer length due to thermal strains in the steel and the LVDT measurements. Thermal strains in the steel were calculated using the linear thermal expansion in (d).

generated until the beginning of the SSPT. During this period, inner mould restraint prevented the outer length from contracting at the same rate as the thermal strain prediction. Although the increase in measured and simulated outer lengths does not necessarily match during the phase transformation, it is unlikely that distortions were generated during this period. As previously stated, differences in the LVDT measurements during the SSPT are likely due to variations in the casting chemistry (see Table 1). After the phase transformation, the LVDT measurements and thermal simulation curve are parallel (i.e. contract at the same rate), signifying that all dimensional changes after the phase transformation are due to thermal strains.

5. Stress model and mechanical properties

5.1. Governing equations and constitutive relations

For the present study, the solid momentum equation neglects inertial effects and momentum transport between the solid and liquid during solidification and reduces to

$$\nabla \cdot \boldsymbol{\sigma} + \rho \boldsymbol{g} = 0 \tag{2}$$

where $\boldsymbol{\sigma}$ is the stress tensor, ρ is the material density, and $\boldsymbol{g}$ is the gravitational acceleration. Using the small strain assumption, the strain tensor ($\boldsymbol{\varepsilon}$) is decomposed into its elastic ($\boldsymbol{e}$), plastic ($\boldsymbol{pl}$), and thermal components ($\boldsymbol{th}$), i.e. $\boldsymbol{\varepsilon} = \boldsymbol{\varepsilon}_e + \boldsymbol{\varepsilon}_{pl} + \boldsymbol{\varepsilon}_{th}$. The elastic strains are determined from Hooke's law assuming the steel and bonded sand are homogeneous and isotropic materials.

The stress model for the steel is based on the implementation by Monroe and coworkers [16,17], in which the mushy zone is treated as a compressible porous medium. In addition, the model considers rate, hardening and temperature effects. The yield stress is defined as
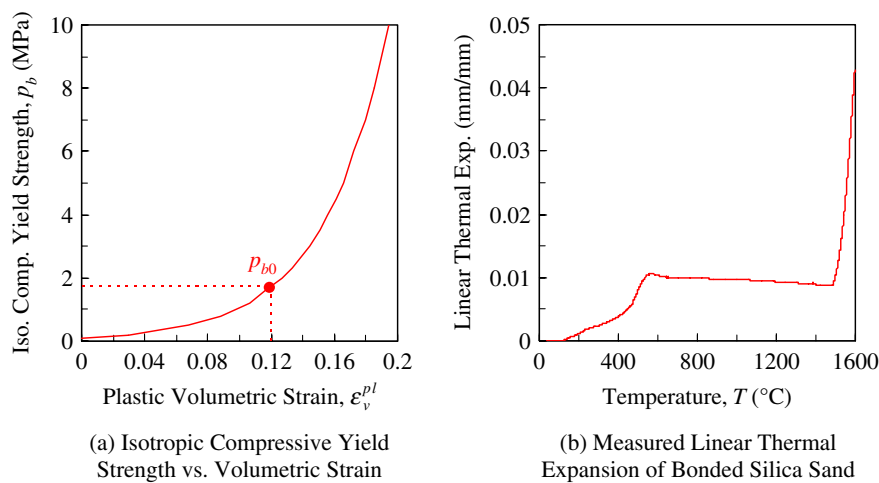
a function of the solid volume fraction, which eliminates the need to model each phase (i.e. fully liquid, fully solid, semi-solid) separately. The coherency solid fraction, g_s^{coh}, represents a transition; below g_s^{coh}, the steel has no tensile strength and is modelled as an elastic material with a low modulus. Above g_s^{coh}, the dendrites form a continuous network, allowing the steel to transmit stresses. At $g_s = 1$, the model reduces to a standard elasto-visco-plastic constitutive law.

The bonded sand is modelled using the Drucker–Prager Cap model from the ABAQUS® material library (named the Extended Drucker–Prager/Cap model in ABAQUS®). A detailed description of the model is given by Galles and Beckermann [1]. The model features pressure-dependent yielding and is commonly used to model geological materials such as sand. The yield surface is comprised of a shear failure surface, cap surface, and transition surface, which smoothly connects the other two surfaces to avoid numerical difficulties. The cap translates with changes in plastic volumetric strain and thus, defines the hardening behaviour. Yielding on the shear failure and cap surfaces results in dilation and compaction, respectively. In addition, non-associated and associated flow rules are employed for the shear failure and cap surfaces, respectively.

5.2. Mechanical properties

For the steel, the temperature-dependent Young's modulus for the steel was taken from Koric and Thomas [18] and a constant Poisson's ratio of 0.3 was used. Temperature-dependent elasto-visco-plastic model parameters were taken from Galles and Beckermann [12].

Bonded sand properties were determined by Galles and Beckermann [1], who used a critical temperature to define the transition from bonded to un-bonded sand, which was caused by pyrolysis of the binder. Room temperature values for the cohesion ($d_{R.T.}$) and Young's

(a) Isotropic Compressive Yield Strength vs. Volumetric Strain

(b) Measured Linear Thermal Expansion of Bonded Silica Sand

Figure 7. The evolution of the hydrostatic compression strength (p_b) in (a) defines the hardening behaviour for the bonded sand. Here, a positive plastic volumetric strain represents a reduction in volume. The initial hydrostatic compressive strength (p_{b0}) was calculated from the initial bulk density. Thermal strains in the bonded sand were predicted using the linear thermal expansion behaviour shown in (b).

Table 2. Mechanical properties and Drucker–Prager Cap parameters for the silica bonded sands.

Temperature (°C)	E (MPa)	v	β	d (MPa)	R	α
20	3403	0.3	55°	1.85	0.45	0.01
180	60	0.3	55°	0.11	0.45	0.01
1600	60	0.3	55°	0.11	0.45	0.01

modulus ($E_{R.T.}$) were linearly degraded to their high temperature values at the critical temperature ($T_{crit} = 180\,°C$) and then held constant. All other properties, including the friction angle ($\beta = 55°$), cap eccentricity ($R = 0.45$), Poisson's ratio ($v = 0.3$), and transition surface parameter ($\alpha = 0.01$) were taken as constants. The elastic mechanical properties and Drucker–Prager Cap model parameters are summarised in Table 2. The position of the cap yield surface on the pressure axis is defined by the hydrostatic compressive yield strength (p_b), which is plotted as a function of plastic volumetric strain in Figure 6(a). The hydrostatic compressive yield strength evolves with changes in plastic volumetric strain increment and therefore, defines the hardening behaviour. The initial hydrostatic compressive yield strength (p_{b0}) is determined from the initial bulk density of the bonded sand. Finally, the linear thermal expansion coefficient of the bonded sand was measured with a dilatometer and is shown in Figure 6(b).
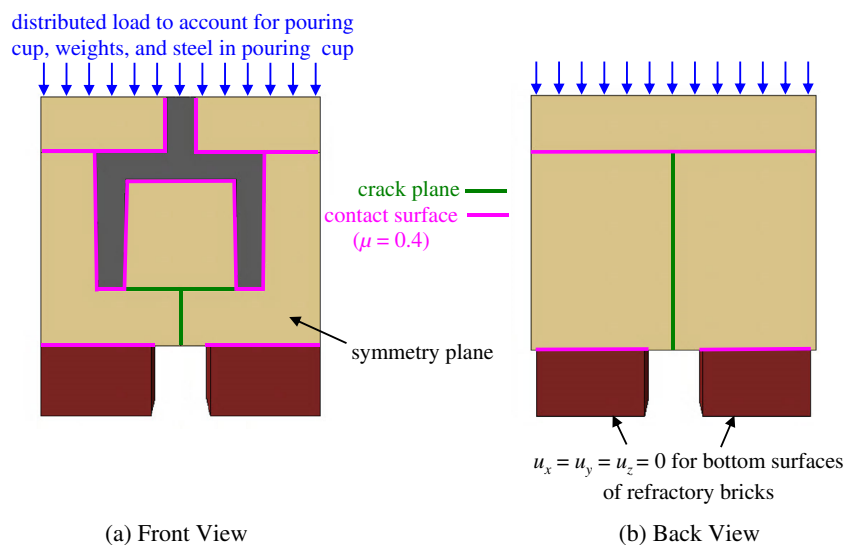
6. Stress simulations

6.1. Procedure and simulation inputs

Stresses and strains in the bracket and mould were calculated using the general purpose finite-element code ABAQUS®.[19] An explicit time integration scheme (i.e. ABAQUS®/explicit) was used for the present study in order to avoid numerical difficulties associated with the material softening that accompanies dilative behaviour.

For this strategy, the time step is conditionally stable and limited by how fast stresses can propagate through the material. The minimum time step is determined by the characteristic element dimension, elastic mechanical properties, and material density. In general, however, this calculation results in a very small time step, which leads to impractical computation times. For quasi-static processes, however, distortions occur at rates much lower than the speed at which the stress wave propagates. For situations such as these, mass scaling is employed in order to increase the stable time increment. A detailed explanation of how the time step is determined can be found in the ABAQUS® documentation.

The finite-element model is depicted in Figure 8. Taking advantage of symmetry, only ½ of the experimental geometry was modelled. A symmetry plane was defined at the vertical casting mid-plane. The general contact algorithm in ABAQUS®/explicit was used to model the interaction between the casting and mould as well as between the mould and refractory bricks (contact surfaces are denoted by pink lines in Figure 8). Friction between the contact surfaces was set to $\mu = 0.4$. The model was constructed using 8-node linear brick elements. The casting and mould consisted of approximately 12,000 and 50,000 nodes, respectively. Simulations were performed on an Intel® Xeon® E5–2687 W v2 processor containing 8 cores with a CPU clock speed of 3.4 GHz. Run times were approximately 8 h. Initially, the crack planes in Figure 8 were not modelled in the stress simulation. The reason for its inclusion in subsequent simulations is explained below.

Inputs for the stress simulations include the elastic mechanical properties and viscoplastic parameters for the steel [12] and bonded sand (given in Table 2), thermal expansion coefficients for the steel (Figure 6(d)) and bonded sand (Figure 7(b)), and the calculated

distributed load to account for pouring cup, weights, and steel in pouring cup

crack plane ——
contact surface ——
($\mu = 0.4$)

symmetry plane

$u_x = u_y = u_z = 0$ for bottom surfaces of refractory bricks

(a) Front View   (b) Back View

Figure 8. General contact modelled interactions between the casting, mould, and refractory bricks (pink lines). Crack planes are denoted by the green lines. A distributed load on top of the cope accounted for the pouring cup, metal in the pouring cup, and weights placed on top of the cope. Using the symmetry plane in (a), only ½ of the geometry was modelled.
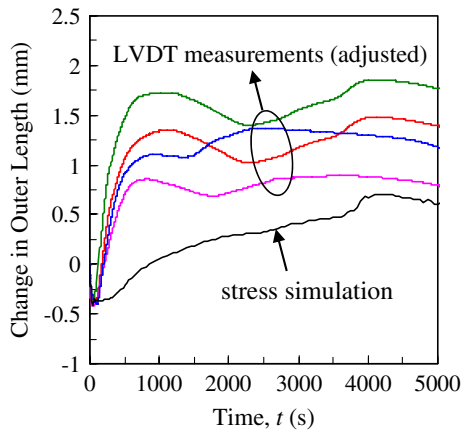
Figure 9. Comparison between the LVDT measurements and the change in outer length predicted by the finite element stress simulation.

temperature fields from MAGMASOFT®. The hardening behaviour of the bonded sand must also be specified and is governed by Figure 7(a), which plots the hydrostatic compressive strength (p_b) of the bonded sand as a function of plastic volumetric strain. In order to determine the initial hydrostatic compressive strength (p_{b0}), the initial bulk density (i.e. packing density) of the bonded sand is also required.[1] Unfortunately, the bulk density was not measured prior to the experiments. Instead, a representative bulk density ($\rho_b = 1710$ kg/m³) was estimated from a hand-packed bonded sand sample. From this initial bulk density, p_{b0} was determined to be 1.7 MPa.

6.2. Stress simulations

Using the inputs, a stress simulation predicted the change in outer length, which is compared to the LVDT measurements in Figure 9. The observed decrease in outer length during the initial 50 s (due to mould expansion) was reasonably predicted, as the stress simulation curve decreases to −0.4 mm. After 50 s, however, the stress simulation curve does not match the LVDT measurements. In particular, the LVDT curves increase at a much higher rate than the stress simulation curve between 100 and 1000 s. In other words, the bracket legs were pushed outward much faster in the experiments than the simulations. Additionally, the observed decrease in the outer length after 1000 s was not predicted. The stress simulation curve is approximately parallel to the red LVDT curve after the onset of the SSPT (SSPT), i.e. the local minimum at 2500 s. However, because distortions were not generated after the SSPT commenced (this was demonstrated by the thermal strain simulations in Section 3), these later times are not particularly interesting. Thus, the finite-element stress simulation could not predict the outer length evolution for the time period during which distortions were observed.
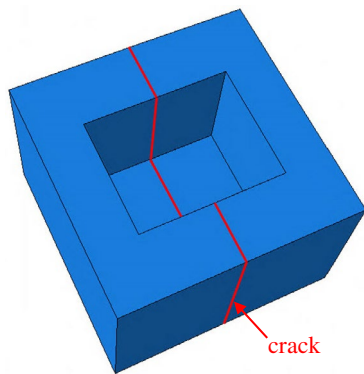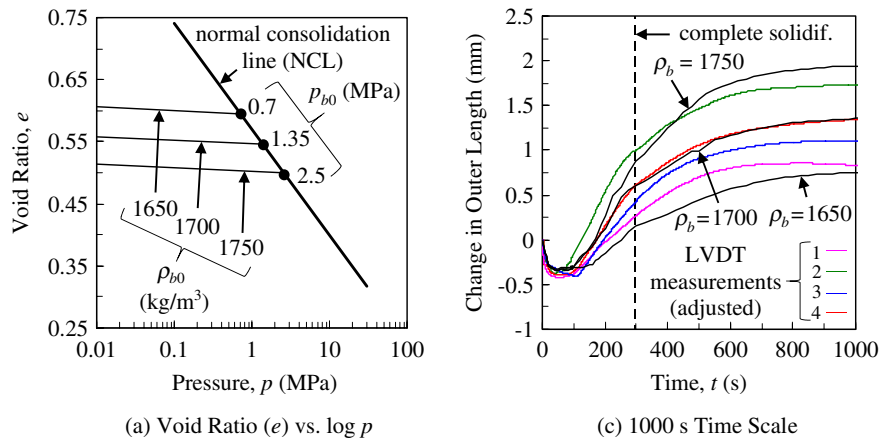

(a) Observed Crack Plane in Drag
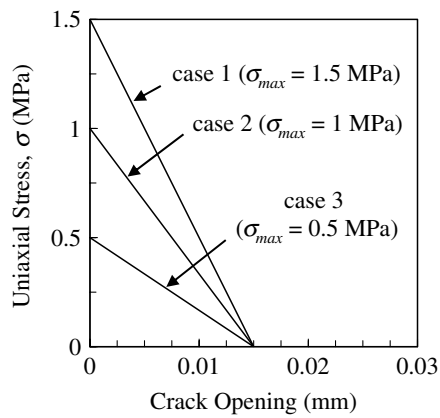
(b) Stress-displacement Behavior after Onset of Crack
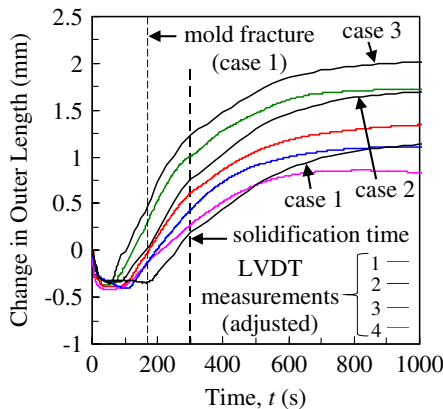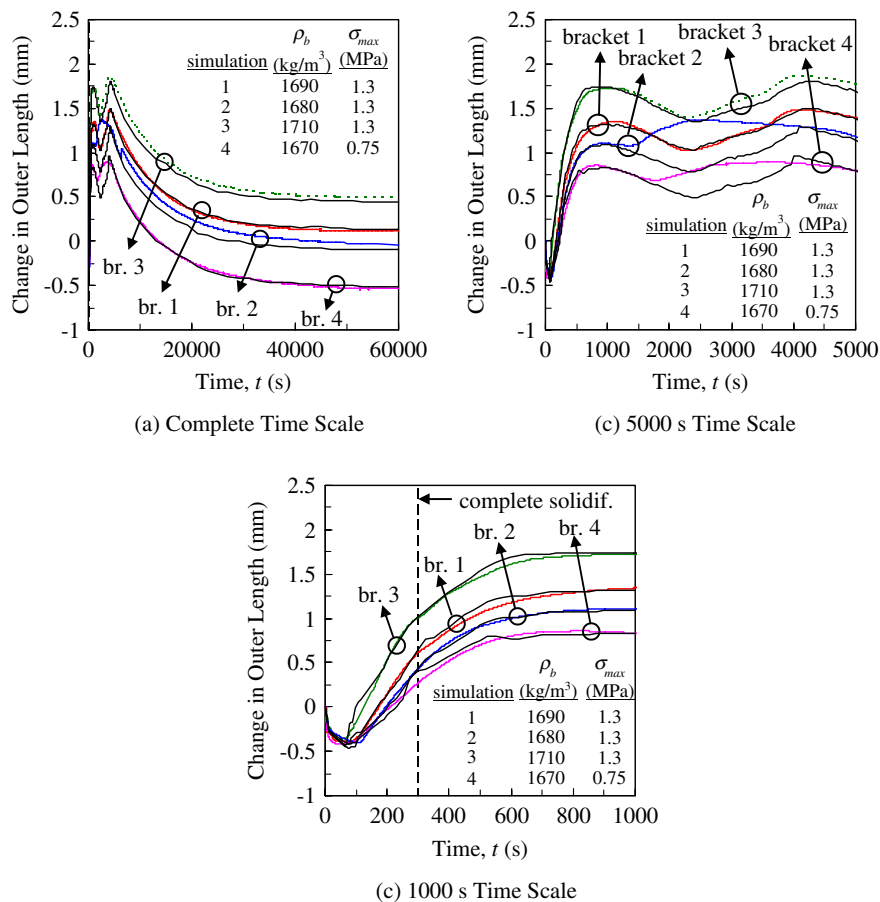

(c) Change in Outer Length

Figure 10. Mould fracture was observed at the location shown in (a). A parametric study demonstrated the effect of the maximum uniaxial stress (σ_{max}) on the predicted change in outer length (c).

Figure 11. A parametric study demonstrated the effect of the initial bulk density of the bonded sand on the predicted change in outer length.

During the experiments, the drag fractured at the location shown in Figure 10(a), shortly after pouring. Until the time of fracture, the tensile strength of the outer mould provided restraint that prevented the bracket legs from being pushed outward. At the time of fracture, however, this strength rapidly deteriorated, which essentially eliminated any restraint. After this, the bracket legs could be easily pushed outward by the thermally expanding inner mould.

To simulate this behaviour, a vertical crack plane was defined in the model at the observed location of fracture using surface-based cohesive behaviour in ABAQUS®/explicit. A horizontal crack plane was also defined between the inner mould and remainder of the drag. Without this additional plane, the two drag halves were held intact by the inner mould and could not separate from each other. Once the tensile capacity in the cohesive bond is reached, the bond degrades as the

Figure 12. Comparison between the measured and predicted (black curves) changes in the outer length for the bracket experiments after adjusting the bulk density (ρ_b) and maximum tensile stress of the crack plane (σ_{max}) for each experiment.
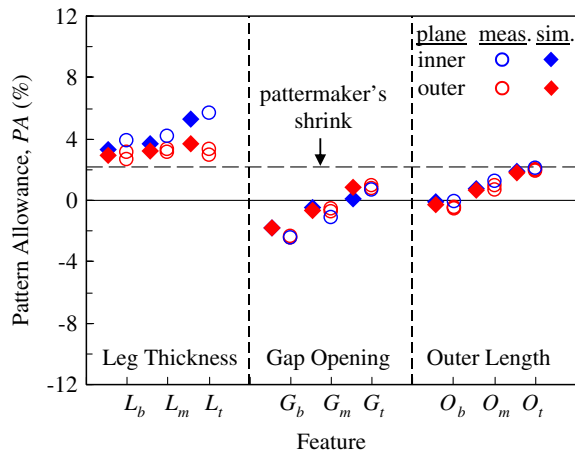
(a) Comparison between Measured and Predicted
Pattern Allowances for Experiment 1
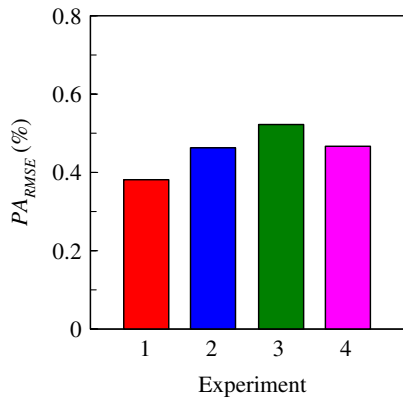
(b) Root Mean Square Error of Pattern
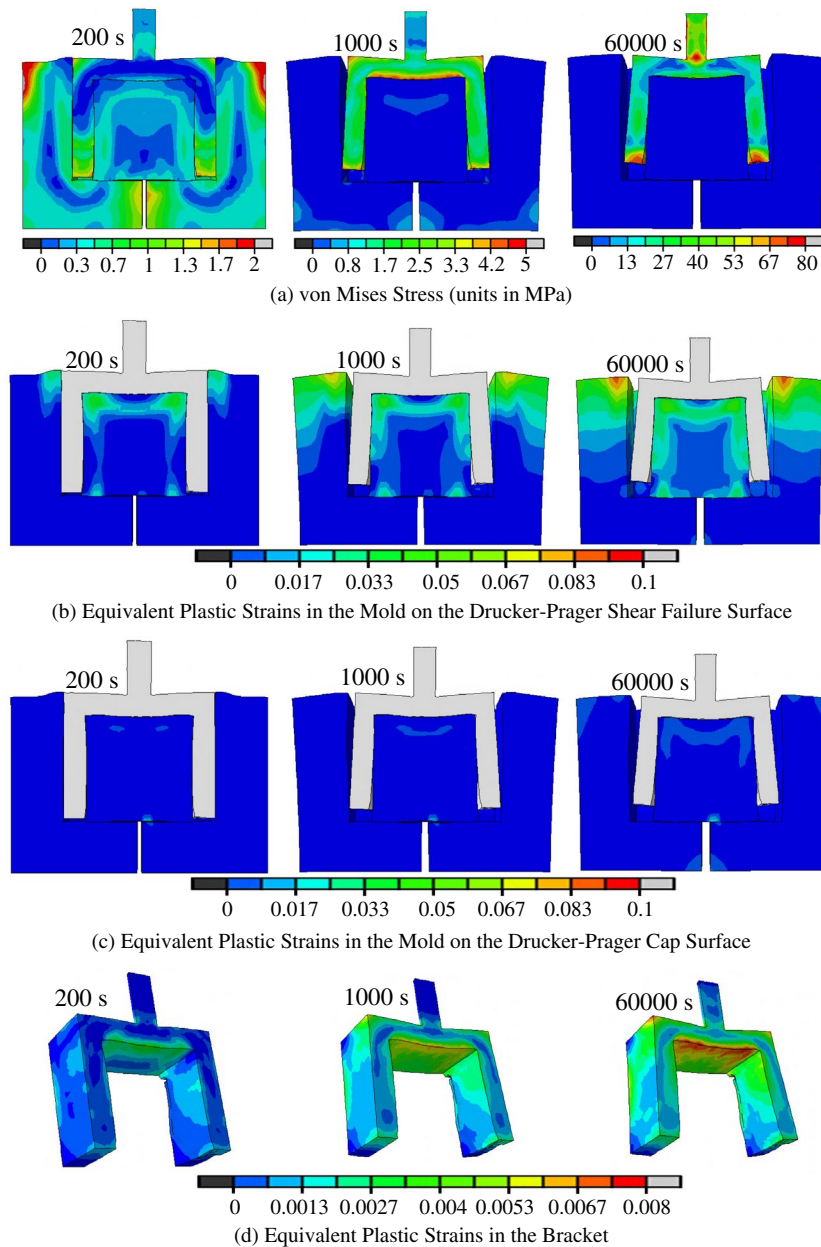Allowances for all Experiments

Figure 13. The predictive capability of the computational model is demonstrated in (a). The RMSEs in (b) range from 0.39 to 0.52% for all experiments.

surfaces are pulled apart. This degradation is governed by stress-displacement behaviour such as that shown in Figure 10(b), in which the tensile strength of the bonded sand linearly decreases from a maximum tensile stress (σ_{max}) to zero at some finite crack opening (0.015 mm for this study). The three cases shown in Figure 10(b) contain different values for σ_{max}. Such variations are needed in order to predict mould fracture at different times (Figure 2(a) illustrates that the experiment 3 mould fractured earlier than those in the other experiments). The curves were based on a uniaxial tensile test performed on a sodium silicate bonded sand by Caylek and Mahnken,[9] who measured a maximum tensile stress of 1.3 MPa. A linear stress-displacement behaviour was employed, which was based on finite-element predictions that the cohesive bond failed in a matter of seconds (<10), regardless of the type of relation (i.e., linear, exponential, power series). Using the curves in Figure 10(b), a parametric study investigated the sensitivity of the predicted outer length evolution to changes in σ_{max}. The tensile strengths in Figure 10(b) were linearly decreased from room temperature to a very small value at the pyrolysis temperature (180 °C for this study), which was determined

from the measured heating curves in the bonded sand. Pyrolysis of the binder is an endothermic reaction that reduces the local heating rate to nearly zero. Results of the parametric study are shown in Figure 10(c). Now it can be seen that the predicted outer lengths increase at rates similar to those observed in the experiments. These increases coincide with the predicted times of fracture and are henceforth referred to as the time of mould fracture. For example, the time of mould fracture for case 1 (175 s) is denoted by a vertical dashed line in Figure 10(c). As σ_{max} decreases, mould fracture is predicted earlier, which in turn leads to larger amounts of distortions. For example, case 3 (σ_{max} = 0.5 MPa) predicts mould fracture at approximately 80 s and a maximum change in outer length of 2 mm at 1000 s. In contrast, case 1 (σ_{max} = 1.5 MPa) predicts mould fracture at a much later time (175 s), resulting in a maximum change of only 1.1 mm at 1000 s. Interestingly, these simulations have shown that the outer mould restraint impeded the pushout of the bracket legs and actually prevented distortions. This counters the intuition that mould restraint always generates distortions.

The inclusion of a crack plane in the finite-element model provides a mechanism for predicting the steep increase that was observed in the outer length, particularly between 100 s and 500 s (see Figure 2(c)). During the experiments, the maximum change in outer length (which occurred at approximately 1000 s) ranged from 0.75 mm (for experiment 4) to 1.75 mm (for experiment 3). By modifying the stress-displacement curves in similar fashion to those in Figure 10(b), these observed variations can now be predicted. However, such modifications may also lead to considerable disagreement between the measurements and predictions at earlier times. This can be seen when comparing the 'case 1' simulation to the experiment 2 LVDT measurement (blue curve) in Figure 10(b). Although both curves show the same change in outer length at 1000 s, the measured outer length begins to increase at 120 s, whereas the predicted outer length increases much later, at 175 s. It is clear that in order to predict the change in outer length for experiment 4 at 1000 s, σ_{max} would have to be further reduced, which would cause the predicted time of mould fracture to occur even later. Therefore, the outer length evolutions cannot be predicted solely through modifications to the stress-displacement curves (that govern the degradation of the cohesive bond). Another mechanism must be considered.

Recall that the moulds for the bracket experiments were hand packed. Using this technique, some amount of variation in the initial bulk density (ρ_{b0}) between the experiments can be expected. The effect of the bulk density on the bonded sand strength is illustrated on the void ratio (e) vs. log p (where p is the pressure) plot shown in Figure 11(a). The nearly horizontal curves are loading–reloading lines and were constructed through

(a) von Mises Stress (units in MPa)

(b) Equivalent Plastic Strains in the Mold on the Drucker-Prager Shear Failure Surface

(c) Equivalent Plastic Strains in the Mold on the Drucker-Prager Cap Surface

(d) Equivalent Plastic Strains in the Bracket

Figure 14. Predicted von Mises stresses (a) and equivalent plastic strains (b–d). Distortions are magnified by a factor of 5.

a procedure described by Galles and Beckermann.[1] The intersection of the loading–reloading lines and the normal consolidation line (NCL) define the initial hydrostatic compressive strength (p_{b0}) of the bonded sand. From the figure, it can be seen that as the initial bulk density increases, p_{b0} also increases. Intuitively, this makes sense; a densely packed sand has a higher compressive strength than a loosely packed sand. Therefore, the effect of the initial hydrostatic yield stress was investigated through a parametric study, in which the change in outer length was predicted using the p_{b0} values shown in Figure 11(a) (i.e., 0.7 MPa, 1.35 MPa, and 2.5 MPa). To model the degradation of the cohesive bond, the 'case 2' curve in Figure 10(b) was used. Results are shown in Figure 11(b). Clearly, different initial bulk densities have a large impact on the predictions, as the predicted change in outer length varies from 0.5 mm to 2 mm at 1000 s.

The family of predicted curves in Figure 11(b) looks similar to the predictions in Figure 10(c) with one important exception; the magnitudes of the curves are now independent of the mould fracture time. This is in contrast to the previous parametric study, in which variations in σ_{max} affected both the magnitudes of the predicted curves and times of mould fracture. This notable difference provides the means needed to predict the observed outer length evolution.

In order to match the measured and simulated changes in outer lengths, the maximum uniaxial stress was first adjusted so that the measured and simulated mould fracture times were matched. As in the parametric study, the tensile strength was linearly decreased from σ_{max} to zero at a crack opening of 0.015 mm. Then, the density was adjusted (which affected p_{b0}) so that the correct magnitude of pushout was predicted. The results are shown on

complete (a), 5000 s (b), and 1000 s (c) time scales in Figure 12. The maximum tensile stress and bulk densities used for the simulations are listed for each experiment within the figures. Now, the measurements and simulations are in excellent agreement at all times, with the exception of experiments 2 (blue curve) and 4 (pink curve) between 1500 s and 4000 s. The disagreement at these times is likely due to differences in the casting chemistries (see Table 1) that caused variations in the time and duration of the SSPT. During this time period, the measured and predicted curves first diverged but eventually converged again. By modifying the kink in Figure 6(c) for each individual experiment, the disagreements during the SSPT could have been eliminated. However, this added effort would not have affected the pattern allowance predictions, and therefore, was not performed.

Pattern allowance comparisons for experiment 1 are shown in Figure 13(a). In general, the predictions (solid diamond symbols) are in excellent agreement with the measurements (hollow circular symbols). In addition, the bias seen between the inner plane (blue) and outer plane (red) PA for the leg thicknesses (L) were predicted. In order to quantify the error for the predicted PA, the root mean square error (RMSE) was calculated for each experiment and is shown in Figure 13(b). PA$_{RMSE}$ varied from 0.39% (experiment 1) to 0.52% (experiment 3). For comparison, using the patternmaker's shrink gives a RMSE of greater than 2%.

Predicted von Mises stresses and equivalent plastic strains in the casting and mould for experiment 1 are shown in Figure 14. Distortions are magnified by a factor of 5. At 200 s, mould fracture has already occurred, as a gap can be seen between the two drag halves. The bracket legs are clearly pushed outward at 1000 s. Note that different stress scales are used for each time in Figure 14(a). Figure 14(b) and (c) show the predicted equivalent plastic strains in the mould due to yielding on the shear failure and cap surfaces, respectively. Therefore, the contours in Figure 14(b) and (c) indicate sand dilation and sand compaction, respectively. For the inner mould region, shear stresses such as those in Figure 14(a) at 200 s were necessary to predict the large amounts of equivalent plastic strains associated with the shear failure surface (Figure 14(b)). The minimal amount of equivalent plastic strains predicted on the cap surface imply that very little compaction was predicted for the inner mould. However, this is not to say inner mould restraint was unimportant. Likely, the compressive strength of the inner mould was already sufficient to provide considerable restraint and generate distortions. The largest amounts of equivalent plastic strains in the bracket were predicted on the bottom surface of the top section, at the mid-plane (see Figure 14(d)). This coincides with the maximum stresses predicted in the bracket (see Figure 14(a) at 1000 s). The von Mises stresses in the bracket at 60,000 s represent the residual stresses, which average roughly 40 MPa throughout the bracket with some localised regions approaching 80 MPa.

7. Conclusions

This study investigated the dimensional inaccuracies that arise from mechanical interactions during sand casting. Casting experiments involving a U-shaped steel bracket were performed and then simulated in order to study the effect of such interactions on PA. The temporal evolution of the gap opening between the bracket legs was measured *in situ* and revealed that mould restraint generated considerable distortions after solidification. Distortions were also created by mould expansion during solidification. Mould fracture was observed during the experiments approximately 100 s after filling. It was later revealed during the stress simulations that unless this fracture behaviour was considered, the tensile strength of the outer mould impeded the pushout of the bracket legs and distortions were under-predicted. To account for this effect, surface-based cohesive behaviour was utilised to model mould fracture. Finally, it was found that the significant variations in the LVDT measurements could be predicted through modest changes to the packing density of the moulds.

The present study is the culmination of an effort to predict PA for steel sand castings. It is envisioned that the current computational model will drastically reduce lead times as well as reduce dimensional variations in the as-cast part. Most importantly, because the simulations were performed using commercial software, the procedures outlined in this study can be easily duplicated. This gives the foundry engineer the necessary tools to minimise distortions and predict PA efficiently and accurately.

Disclosure statement

No potential conflict of interest was reported by the authors.

References

[1] Galles D, Beckermann C. Int J Cast Metals Res. Effect of sand dilation on distortions and pattern allowances during steel sand casting. Submitted for publication.

[2] Parkins RN, Cowan A. Effects of mould resistance on internal stress in sand castings. Proceedings of the Institute of British Foundation, paper No. 1062; 1953. p. A101-9.

[3] Mkumbo CSE, Nyichomba BB, Campbell J, Tiryakioglu M. Linear contraction of grey iron sand castings. Int J Cast Metals Res. 2002;14:225–234.

[4] Nyichomba BB, Cheya IM, Campbell J. Linear contraction of ductile iron castings. Int J Cast Metals Res. 1998;11:179–186.

[5] Nyichomba BB, Campbell J. Linear contraction and residual stress of aluminum alloy sand castings. Int J Cast Metals Res. 1998;11:163–167.

[6] Motoyama Y, Takahashi H, Inoue Y, Shinji K, Yoshida M. Development of a device for dynamical measurement of the load on casting and the contraction of the casting in a sand mold during cooling. J Mater Process Tech. 2012;212:1399–1405.

[7] Peters F, Voight R, Ou SZ, Beckermann C. Effect of mould expansion on pattern allowances in sand casting of steel. Int J Cast Metals Res. 2007;20:275–287.

[8] Yamamoto O, Yamada H, Saito M. Properties of furan and oil-urethane nobake binder at room and elevated temperatures. Jpn Foundry. 1978;50:14–18.

[9] Caylek I, Mahnken R. Thermomechanical characterisation of cold box sand including optical measurements. Int J Cast Metals Res. 2010;23:176–184.

[10] Thole J, Beckermann C. Measurement of elastic modulus of PUNB bonded sand as a function of temperature. Int J Metalcast. 2010;4:7–18.

[11] Saada RA, Bonnet G, Bouvard D. Thermomechanical behavior of casting sands: experiments and elastoplastic modeling. Int J Plast. 1996;12:273–294.

[12] Galles D, Beckermann C. In-situ measurement and prediction of stresses and strains during casting of steel. Metall Mater Trans A. 2016;47A:811–829.

[13] MAGMA GmbH, MAGMAsoft, Kackerstrasse 11, 52072 Aachen, Germany.

[14] Galles D, Beckermann C. Measurement and simulation of distortion of a steel bracket casting. 66th Steel Founders Society of America Technical and Operating Conference, Paper No. 5.2. Chicago (IL): Steel Founders' Society of America; 2012.

[15] Carlson KD, Beckermann C. Determination of solid fraction-temperature relation and latent heat using full scale casting experiments: application to corrosion resistant steels and nickel based alloys. Int J Cast Metals Res. 2012;25:75–92.

[16] Monroe C. [PhD thesis]. A modeling and experimental study of deformation and hot tearing in steel. Iowa City (IA): University of Iowa; 2009.

[17] PokornyM, Monroe C, Beckermann C. Prediction of hot tear formation in a magnesium alloy permanent mold casting. Int J Metalcast. 2008;2:41–53.

[18] Koric S, Thomas BG. Efficient thermo-mechanical model for solidification processes. Int J Numer Methods Eng. 2006;66:1955–1989.

[19] ABAQUS®. Abaqus, Inc., Providence, RI.